Numerical Validation of CHT method for simulation of Anti-/de-Icing Piccolo System

Ridha Hannat[1] and François Morency[2]
École de Technologie Supérieure, Montréal, Québec, H3C 1K3, Canada

Anti-/de-icing CHT method based on ANSYS-CFX flow solver and FENSAP-ICE software is presented. The ANSYS-CFX flow solver is used as the flow solver module with the $k-\omega$ SST turbulence model. DROP3D is used as the droplet impingement module. ICE3D is used as the ice accretion and water film runback module. CHT3D/CFX is used for the thermal coupling of all modules. Before solving for the temperature distribution in a 3D anti-icing system geometry based on a piccolo tube with three jet rows, a test case consisting of a two stream parallel gas to gas micro heat exchanger will validate the CHT3D/CFX procedure. For the anti-icing system in wet air mode temperature results at corresponding experimental locations are presented and compared to results from literature.

Nomenclature

AOA	=	angle of attack (degrees)
C_D	=	air droplet drag coefficient
C_w	=	specific heat at constant pressure for water (J kg^{-1} K^{-1})
c	=	chord (m)
d	=	nozzle diameter (m)
Fr	=	Froude number
GCI	=	Grid Convergence Index
g	=	gravity (m s^{-2})
h	=	specific enthalpy (J kg^{-1})
h_f	=	film thickness (m)
h_{tot}	=	total specific enthalpy (J kg^{-1})

---

[1] Ph. D. Student, Mechanical Engineering , 1100 Notre-Dame Ouest/ ridha.hannat.1@ens.etsmtl.ca
[2] Professor, Mechanical Engineering, 1100 Notre-Dame Ouest/ Francois.Morency@etsmtl.ca, AIAA Member.

I	=	turbulent intensity
K	=	droplet inertia parameter
k	=	turbulence kinetic energy (m^2 s^{-2})
k_f	=	fluid thermal conductivity (W m^{-1} K^{-1})
k_s	=	solid conductivity (W m^{-1} K^{-1})
LWC	=	liquid water content (g m^{-3})
MVD	=	median volumetric diameter (μm)
$\dot{m}_{jet}$	=	mass flow rate at jet inlet (kg s^{-1})
Nu	=	local Nusselt number $(Q_\text{w}\, d/\, ((T_{wall}\text{-}T_{0,\text{jet}})\, k_f))$
$\overline{Nu}$	=	average Nusselt number
Pr	=	Prandtl number $(\mu\, cp/k_f)$
p	=	pressure (Pa)
Q_S	=	conduction heat flux from the wall in the normal direction η (W m^{-2})
q_w	=	wall heat flux (W m^{-2})
Re	=	jet Reynolds number $(\rho\, U\, d\, \mu^{-1})$
Re$_D$	=	droplet Reynolds number
R_s	=	gas constant (J kg^{-1} K^{-1})
r	=	airfoil radius at leading edge (m)
s	=	curvilinear distance (m)
T	=	temperature (K)
T_b	=	bulk temperature (K)
T_{wall}	=	wall temperature (K)
$T_{0.\text{air}}$	=	free stream temperature (K)
$T_{0,\text{jet}}$	=	total temperature at jet inlet (K)
T^+	=	dimensionless temperature
t	=	time (s)
U	=	mean velocity (m s^{-1})

u = velocity components in x direction (m s^{-1})

u_a = dimensionless air velocity

u_d = dimensionless droplet velocity over a small fluid element around the location x at time t

u_f = velocity of the water in the film (m s^{-1})

$\overline{u_f}$ = mean velocity of the water in the film (m s^{-1})

V_{air} = free stream velocity (m s^{-1})

w = relaxation parameter

α = mean value of the dimensionless water volume fraction

Δy = distance from the wall

ε = relative error

μ = laminar dynamic viscosity (kg m^{-1} s^{-1})

μ_t = turbulent viscosity (kg m^{-1} s^{-1})

η = normal vector

ρ = density (kg m^{-3})

ρ_a = air density (kg m^{-3})

ρ_w = water density (kg m^{-3})

τ = molecular stress tensor (Pa)

ω = specific dissipation (s^{-1})

I. Introduction

ARRAYS or lines of impinging jets provide a simple and efficient way to cool down or warm up surfaces. In aeronautics, cold impinging jets cool the fan blades inside turbines and hot impinging jets protect wing leading edges and engine inlets from ice accretion during flight. Hot jets make it possible to build simple and cost effective in flight ice protection systems for aircraft. Bleed air from jet engines provides the air at high temperature and pressure needed for the jets. Large piccolo tubes with one or more rows of small diameter exit holes distribute hot air at temperatures ranging as high as 250°C [1] to protect aircraft areas such as wing leading edges or nacelle lips. Cooled hot air leaves the protected area through discharge holes in a plenum beam, the front wing spar or the metal skin.

The mass flow rate of extracted hot compressed air must be kept as low as possible, however, because extracting air reduces the efficiency of turbofan engines. Proper design of anti-icing devices consequently requires accurate evaluation of heat flux through the leading edge metal skin. Experimental or Computational Fluid Dynamic (CFD) studies may be used to evaluate heat flux in proposed designs. CFD studies cost less than experimental studies and are therefore attractive. CFD tools can also be used together with optimization methods to design future anti-icing device geometries.

The CFD tools used for the present studies include FENSAP-ICE and ANSYS CFX. FENSAP-ICE is a second generation icing simulation system, meaning that CFD solves the entire icing problem. It was developed during last decade. First, in 1999, an Eulerian model for air flows containing water droplets was proposed as an alternative to the traditional Lagrangian particle tracking approach to compute droplet impingement on airfoils [2]. The model was implemented in a 3D droplets Eulerian code, DROP3D, used for computing the water caught on 3D aircraft components and engines. In 2000 [3], a thermodynamic model for ice accretion on three-dimensional lifting surfaces, including water runback effects, was implemented into the new code ICE3D. This model was originally called Shallow-Water Icing Model or SWIM. ICE3D's physical model essentially consists of converting the classical Messinger model into a PDE system of conservation equations. In 2003 [4] a roughness calculation was implemented in the Spalart–Allmaras (S–A) one-equation turbulence model of FENSAP airflow solver to have reliable ice accretion simulations. In 2004, for the first time a full three-dimensional helicopter icing simulation system was evaluated with FENSAP-ICE [5]. Improvements were made in DROP3D in 2006 to consider ice accretions resulting from supercooled large droplets. An Eulerian model of the droplet–wall interaction process was implemented. This model includes splashing and bouncing phenomena [6]. In 2010, a predictive model for roughness evolution in both space and time during in-flight icing was developed. In the same year, a new artificial viscosity method (ISOD) based on diffusion along isovalues surfaces is used [7] was introduced to avoid numerical oscillations in the airflow solution.

In the present work, ANSYS CFX flow solver is used instead of FENSAP airflow solver. With ANSYS-CFX 12.1, it is possible to use k-ω SST turbulence model for internal flow calculation, a model that gives acceptable results for RANS simulation of impinging jet [8]. The k-ω SST turbulence model of ANSYS-CFX was widely studied for impinging jets in an earlier study [9] and therefore it is used in this paper. Even if LES turbulence model could have given better heat transfer prediction, it was not suitable to resolve the 3D test case studied in this paper

for two important reasons. First, for LES simulation, the correct turbulence structure at jet inlet must be known. This is not the case because the flow is not fully developed at jet entrance. Second, the internal piccolo tube could have been considered in the calculation domain, but then the symmetry boundary conditions cannot be used on domain boundary. Hence, the number of nodes would increase drastically and hence the computational cost too, beyond the point of acceptability for optimization in an industrial context.

ANSYS-CFX 12.1 is coupled to FENSAP-ICE's conjugate heat transfer module, CHT3D, to compute heat transfer through wing metal skin. To validate the new conjugate heat transfer procedure, CHT3D/CFX, real airfoil geometry with anti-/de-icing piccolo system is chosen from the literature.

Brown et al.[10] use 2D experiments to propose a correlation for heat transfer in an aircraft nacelle anti-icing system. Average Nusselt number is correlated with the jet diameters and the mass flow rate per unit area of the impinging jet. Nacelle skin shape is not given. In 1998, Croce et al.[11] used CFD to study heat transfer occurring inside a slat geometry. Using a Navier-Stokes flow solver, the authors studied effects of several boundary conditions on metal skin temperature distribution and showed that piccolo tube surface temperatures contribute significantly to heat transfer. Internal flow consists of a single row of impinging jets with a discharge hole on the lower side of the slat, but no geometrical dimensions are given. Fregeau et al.[12] and Saeed [13] use commercial CFD flow solver to study parametric model of anti-icing system piccolo tube system with a curved impingement surface. A one equation turbulence model was used to compute the wall heat transfer. Morency et al.[14] simulate two geometries and three Reynolds numbers. The geometry of the test case represents an airfoil leading edge. A commercial flow solver with the $k-\omega$, $k-\omega$ SST and BSL Reynolds stress turbulence models compute heat transfer from impinging jets to curved surfaces. Computed Nusselt numbers agree among turbulence models and dependence on Reynolds numbers agree with experimental results.

Papadakis et al.[15] generate an experimental database for validation of simulation tools used to design and analyze thermal ice protection system. A straight wing model was used. Cold hold and descent cases were investigated. A test matrix combined two piccolo tube configurations, and a range of bleed-air mass flows and temperatures for dry and wet external flow conditions. Experimental results show an increase in ice shape size and an upstream displacement of the ice front location as the heat supplied to the bleed-air system was reduced.

To perform design and optimization of a 2D bleed-air ice protection system, Domingos et al.[16] computed leading edge skin temperature and runback ice location. They developed a numerical tool that combines data from a

commercial CFD solver for external flow field, and heat transfer correlation for internal flow heat transfer. Their computational results agree well with experimental data from icing tunnel. The airfoil shape is not specified.

To validate LEWICE 2.2 software, Ghenail et al.[17] analyze ice accretion under a wide range of icing conditions and using several airfoils. They did not solve the hot bleed air airflow but assume two-dimensional transient icing with electrical heater input. Thermal analysis shows that numerical results didn't agree with experimental data. Wright [18] evaluates applicability of correlations added to LEWICE software to simulate heat transfer from a piccolo tube anti-icing system. External warm and cold temperature conditions with the same air flow rate were used. The numerical model uses an airfoil similar to the NACA 23014 used in experiments. Numerical results obtained with three rows of round jets are compared with experimental data. The correlations over predict surface temperatures and subsequently, the computed ice residual patterns are different from experimental shapes. Geometry and test conditions were provided.

Carlos et al.[19] proposed a new formulation to simulate the ice accretion in presence of anti-icing system. Carlos et al.[19] use heat transfer coefficient obtained from Wright[18] and their results agree with numerical results of Wright.

To predict the temperature distribution of an aero-engine strut in ice accretion condition, Dong et al .[20] use CFD code and correlation equation to estimate the heat transfer coefficient. The anti-icing system uses hot oil instead of hot air. The mean temperature drop on the strut surface is acceptable when compared to experimental data. To help in desig, Pourbagian et al [21] study the external parameters in flight icing conditions on the energy requirement of in-flight ice protection systems. Hot air or electro-thermal can be used as anti-icing systems by keeping the airfoil surface temperature at constant value.

The main objective of the present paper is to validate the new procedure, CHT3D/CFX, using numerical calculations done with ANSYS CFX 12.1 and FENSAP-ICE. First, FENSAP-ICE and CHT3D/CFX are briefly described. Mathematical models and numerical methods used for the CFD computations are also described. Since CHT3D/CFX uses ANSYS CFX 12.1 as the flow solver, ANSYS CFX 12.1 results will be validated with a compressible 2D flow test case selected from Miwa paper [22]. Then, CHT3D/CFX results for a complex 3D flow with three rows of round jets are compared with experimental and numerical results from Wright [18].

II.   Conjugate Heat Transfer Code

In this section, the exchange of boundary conditions needed for the conjugate heat transfer (CHT) within FENSAP-ICE simulation package's is explained. Then, the ANSYS CFX 12.1 airflow solver and the CHT3D/CFX procedure are presented.

A. CHT within FENSAP-ICE

A brief description of CHT methodology used in FENSAP-ICE is presented. For more details, the reader can consult the paper by Reid et al.[23]. FENSAP-ICE software is mainly used for 3D simulations of in-flight icing phenomena.

FENSAP-ICE includes five fully integrated modules: FENSAP, DROP3D, ICE3D, CHT3D, and C3D. The flow charts in Fig 1 show the interaction between all modules. Arrows indicate information exchange between modules. The three modules related to external domain are grouped together in a large box for the wet air case. In the classical FENSAP-ICE, the airflow solver used for CHT calculation is FENSAP and with the new formulation, it is ANSYS CFX 12.1. Conjugate heat transfer can be evaluated in two modes: dry air mode or wet air mode, depending on the liquid water content of the external flow. Anti-icing systems should only be used in wet air mode, during an icing event, but for result validations purpose and for maximum wall temperature calculations, the dry air mode is useful.

In dry air mode, on the left of Fig 1, when no water is collected by surfaces, the heat transfer at the fluid-solid interfaces is computed using a conduction code, C3D, and an airflow solver, either ANSYS CFX or FENSAP. FENSAP/CFX computes wall heat fluxes at the solid walls for external flow and internal flow and send them to C3D. C3D computes and returns the updated wall temperatures that are used as boundary conditions into FENSAP/CFX.

In wet air mode, on the right of Fig 1, two additional modules are needed. FENSAP/CFX computes convective wall heat fluxes, wall shear stresses, and external air velocity field. DROP3D uses external air velocity field from FENSAP/CFX. It computes and sends the collection efficiency and droplet impact velocities to ICE3D. ICE3D uses results from DROP3D plus the convective wall heat fluxes and wall shear stresses from FENSAP/CFX external flow results and the temperature calculated by C3D. ICE3D compute the ice thickness, the wall surface displacement, and the external wall heat flux for the given surface temperature distribution. The wall surface displacement may be used to modify the wall geometry to consider ice accretion. The external wall heat flux is used by C3D with the internal

wall heat flux to obtain a new wall temperature. Thus, ICE3D modify the external wall heat flux from the airflow solver before sending it to the conduction code.
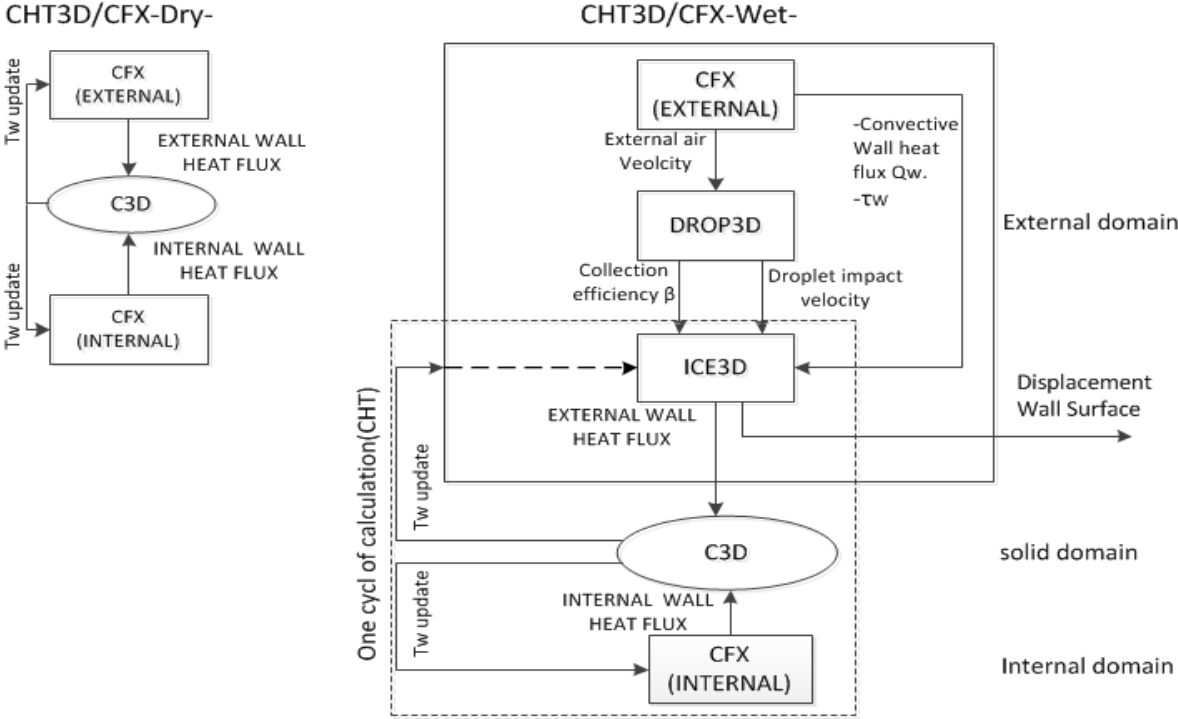

Fig 1   Flow chart for unsteady conjugate heat transfer.

The coupling between the different solutions (internal and external air flows, solid conduction problem) is obtained via an exchange of boundary conditions assumed to be the wall heat flux from airflow solver and the returned wall temperature from solid solver. The wall temperature is updated until steady state is reached. This allows us to define the coupling as a purely interfacial algorithm, independent of the details of the solvers in the different domains.

In the classical FENSAP-ICE, the airflow is modeled with a classical compressible Reynolds averaged Navier-Stokes (RANS) model. The discretized equations are solved using a canonical Galerkin Finite Element discretization[23].

The DROP3D module solves for water concentration and droplet velocities via an Eulerian formulation to automatically determine the mass of water collected on exposed surfaces [2]. The discretized equations are solved using a canonical Galerkin Finite Element discretization. The Eulerian droplet model used in DROP3D is a two-fluid

model consisting of the velocity field for dry air and the droplet-specific continuity and momentum equations(Eq. (1) and Eq. (2). Forces exerted on air by droplet are neglected.

$$\frac{\partial \alpha}{\partial t} + \nabla \cdot (\alpha u_d) = 0 \tag{1}$$

$$\frac{Du_d}{Dt} = \frac{C_D \operatorname{Re}_D}{24K}(u_a - u_d) + (1 - \frac{\rho_a}{\rho_w})\frac{1}{Fr^2}g \tag{2}$$

ICE3D is an ice accretion and water runback module based on the Messinger model [24]. Making the hypothesis that the water runbacks as a continuous film, momentum and energy balances are calculated. An element-based finite volume method is used to compute heat and mass balances in the liquid film. The velocity u_f of the water in the film is assumed to be linear so pressure and gravity effects are neglected [25]. By averaging u_f across the thickness of the film h_f, the mass conservation and energy conservation equations becomes:

$$\rho_w \left[\frac{\partial h_f}{\partial t} + \nabla(\overline{u_f}h_f) \right] = \dot{m}_{imp} - \dot{m}_{evap} - \dot{m}_{ice} \tag{3}$$

$$\rho_w \left[\frac{\partial h_f C_w T}{\partial t} + \nabla(\overline{u_f}h_f C_w T) \right] = E_{imp} - E_{evap} + E_{ice} + Q_h \tag{4}$$

where $\dot{m}_{imp}$, $\dot{m}_{evap}$, and $\dot{m}_{ice}$ are the mass transfer by water droplet impingement, the evaporation, and the ice accretion respectively. E_{imp}, E_{evap}, and E_{ice} are respectively the impinging, the evaporation, and the accretion heat transfer. Q_h is the convective heat transfer. The coefficients ρ_w and C_w represent the physical properties of water. The temperature T is uniform across the water film.

Finally, the heat conduction equation through the solid as well as the melting process in the ice layer models is solved using the 3D heat conduction module C3D, based on a finite element method. Assuming constant thermal conductivities inside solid, C3D solves the Poisson conduction equation in the solid domain:

$$\Delta T = 0 \tag{5}$$

For the conjugate heat transfer calculation, the steady state flow solution is obtained with initial guessed temperature distributions along the walls. The temperature distributions are used as Dirichlet boundary conditions for the flows. Thus at time n, at solid air interface 's':

$$T = T^n \tag{6}$$

The heat flux computed by the Navier–Stokes flow solver is then used as a boundary condition for both solid's sides with a Neumann boundary condition imposed:

$$\frac{\partial T}{\partial \eta} = -\frac{Q_s}{k_s} \tag{7}$$

The solid conduction problem solves the Poisson conduction equation in the solid domain, which then update the temperature distribution on the wall:

$$T^{n+1} = (1-w)T^n + wT_s \tag{8}$$

To start the conjugate heat transfer calculations, the steady-state airflow solutions computed in the external and the internal computational domains are used. The water droplet equations are then solved to obtain the mass of water collected over the exposed surfaces. Finally, the unsteady CHT loop is started: at each time step, Newton iterations are performed using energy equation until the heat fluxes through the interfaces of the various computational domains are conserved, within a given level of accuracy. The ice shapes are then computed according to the net mass growth from the film and shrinkage resulting from melting, for a given time step. The ice-modified geometry is subsequently re-meshed before another steady-flow airflow solution is obtained to start a new cycle of conjugate heat transfer calculations.

B. ANSYS CFX

The new procedure FENSAP/CFX uses ANSYS CFX 12.1 [26] to solve the unsteady Navier-Stokes equations for the hot air internal flow inside the wing and the external flow. The RANS equations are solved to obtain the wall heat flux. The compressible RANS equations are, for eddy viscosity based turbulence models:

$$\frac{\partial \rho}{\partial t} + \nabla \cdot (\rho \mathbf{U}) = 0 \tag{9}$$

$$\frac{\partial \rho \mathbf{U}}{\partial t} + \nabla \cdot (\rho \mathbf{U} \times \mathbf{U}) = -\nabla p + \nabla \cdot ((\mu + \mu_t)(\nabla \mathbf{U} + (\nabla \mathbf{U})^T)) \tag{10}$$

$$\frac{\partial (\rho h_{tot})}{\partial t} - \frac{\partial p}{\partial t} + \nabla \cdot (\rho \mathbf{U} h_{tot}) = \nabla \cdot \left(k_f \nabla T + \frac{\mu_t}{\mathrm{Pr}_t} \nabla h \right) + \nabla \cdot \left(\mathbf{U} \cdot (\tau - \rho \overline{u \times u}) \right) + S_E \tag{11}$$

The viscous work $\nabla \cdot \left(\mathbf{U} \cdot (\tau - \rho \overline{u \times u}) \right)$ is considered in the energy equation Eq. (11) and the source term S_E is neglected. The k-ω SST turbulence model used for turbulent viscosity calculation is presented by Eq. (12) and Eq. (13). This model is detailed in Menter [27]:

$$\frac{\partial (\rho k)}{\partial t} + \nabla \cdot (\rho \mathbf{U} k) = \tilde{P}_k - \beta^* \rho k \omega + \nabla \cdot \left[(\mu + \sigma_k \mu_t) \nabla k \right] \tag{12}$$

$$\frac{\partial (\rho \omega)}{\partial t} + \nabla \cdot (\rho \mathbf{U} \omega) = \alpha \rho S^2 - \beta \rho \omega^2$$
$$+ \nabla \cdot \left[(\mu + \sigma_\omega \mu_t) \nabla \omega \right] + 2(1 - F_1) \rho \sigma_{w2} \frac{1}{\omega} \nabla k \nabla \omega \tag{13}$$

The turbulent eddy viscosity is defined as:

$$v_t = \frac{a_1 k}{\max(a_1 \omega, SF_2)} \tag{14}$$

where S is the invariant measure of the strain rate, F_1 and F_2 are the blending functions, $\tilde{P}_k$ is the production limiter used in the SST model to prevent the build-up of turbulence in stagnation regions and value for constants for β^*, α, σ_k, σ_ω are found in Menter [27].

The fluid is air and its properties follow the ideal gas law:

$$p = \rho R_s T \tag{15}$$

ANSYS-CFX 12.1 uses a collocated finite volume method to solve Eqs (9), (10) (11), (12) and (13). The gas law Eq. (15) relates density to pressure and temperature. From Eq. (9) and Eq. (10), a coupled system of linearized equation is built and solved. Using the velocity field, the energy Eq. (11) and the turbulence model Eq. (12) and Eq. (13) are then solved sequentially. The linearized equations are solved using an algebraic multi-grid method. The system of equations is solved iteratively until the normalized residual of each equation falls below a level set by the user. For the presented test case, the residuals are below 10^{-6} for the internal flow and 10^{-8} for the external flow.

The ANSYS-CFX12.1 blend factor advection scheme [26], with a value 0.75, is used for the calculations to avoid meaningless oscillations in the numerical solution. With a value of 0.75, near second order solution is achieved, without introducing local artificial oscillation.

1) Automatic near wall treatment

ANSYS CFX 12.1 flow solver is used to predict accurate heat transfer on the solid-fluids interfaces in CHT3D/CFX. It uses a special formulation to ensure a smooth shift between the logarithmic wall function approach, and the low Reynolds number formulation based on the near wall mesh spacing [26]. On wall nodes, the flux for the k equation is kept artificially at zero and the flux for the momentum equation is computed from the velocity profile.

For the ω equation, an algebraic expression is specified. It is a blend between the analytical expression for ω in the logarithmic region, and the corresponding expression in the sub-layer.

With this formulation, the location of the first mesh point moves virtually down through the viscous sublayer as the mesh is refined in the low-Reynolds mode. In this study, y^+ values are kept below two for the walls where the heat transfer coefficient is evaluated, and thus a low-Reynolds number formulation is used.

2) Wall heat flux

The thermal law-of-the-wall function of Kader [26] models the thermal boundary layer. The non-dimensional temperature distribution is:

$$T^+ = \Pr y^* \exp(-\Gamma) + \left(2.12 \ln y^* + \beta_T\right) \exp(-1/\Gamma) \tag{16}$$

where:

$$\beta_T = (3.85 \Pr^{1/3} - 1.3)^2 + 2.12 \ln(\Pr) \tag{17}$$

$$\Gamma = \frac{0.01 \left(\Pr y^*\right)^4}{1 + 5 \Pr^3 y^*} \tag{18}$$

$$y^* = \frac{\rho u^* \Delta y}{\mu} \tag{19}$$

For a near wall fluid temperature T_f, the wall heat flux becomes:

$$q = \frac{\rho c_p u^*}{T^+} (T_{wall} - T_f) \tag{20}$$

C. CHT3D/CFX

The new procedure CHT3D/CFX replaces CHT3D and uses three of the four classical modules, the airflow solver FENSAP being replaced by the ANSYS CFX 12.1 airflow solver [26]. The resulting anti-/de-icing CHT procedure is called CHT3D/CFX in this paper. The 3D heat conduction module C3D models the heat conduction through the solid and the melting process in the ice layer, as usual, but instead of extracting data from FENSAP solutions, it extracts data from ANSYS CFX 12.1 solutions.

The CHT3D/CFX procedure needs three files for each fluid domain from ANSYS CFX. The first one is the converged airflow solution file (*.res) providing heat fluxes. The second is the solver input file definition file (*.def) used for batch mode execution. The third is the boundary condition file (*.ccl), containing settings that reference mesh region and physics for a simulation. Finally, the grid solid is used in C3D format grid file.

Steady airflow solutions for internal and external flows from ANSYS CFX 12.1 are used in CHT3D/CFX. For the conjugate heat transfer calculations there is no need to solve the complete RANS system for both internal and external flow. The velocity fields are held constant. Thus, ANSYS CFX 12.1 solves only the energy equation in the external and internal flow computational domains during the CHT iteration.

III. Proposed Test Cases

The first test case proposed is a 2D parallel flow heat exchanger with compressibility effects in one passage, as the compressible flow inside a piccolo tube anti-icing system. The test case is selected from the work of Miwa [22], where a two stream parallel gas to gas micro heat exchanger is numerically studied. It consists of two parallel flows separated by a thin solid interface. Gravity and buoyancy forces are neglected. The geometry is illustrated on Fig 2 where the hot passage is in the upper channel (with subscript H) and the cold passage is in the lower channel (with subscript C). A thin solid interface between the two passages is used to ensure a temperature variation in the x-direction and almost no temperature variation in the y-direction inside the plate. Several solid interface thicknesses are used, ranging from zero thickness to 5 μ. The vertical sides of the solid interface are adiabatic. Each passage has a length of 12.7mm and a width h of 0.05mm. The computational domain is discretized in 400×20 uniform hexahedral cells, a relatively coarse mesh. For the grid convergence study, meshes of 800×40 and 1200×60 hexahedral cells are also used.

For the zero thickness solid interface, two simulations are performed, one with a high velocity (compressible flow) and a low velocity (incompressible flow) in upper and lower passage respectively; the second one with a low velocity in both channels. A constant velocity in the x direction is imposed at inlet for both passages. For the first simulation, the upper passage has a constant stagnation temperature of 350 K at inlet and the Reynolds number is 1326.4 to ensure a Mach number of 0.622 at the upper exit. The Reynolds number is based on average flow rate, and hydraulic diameter at a cross section of a passage. The Mach number is based on the average velocity and temperature at the cross section of a passage. For the lower passage, a constant stagnation temperature of 300 K is imposed at inlet and the Reynolds number is 163.6 to ensure a Mach number of 0.080 at the lower exit. For the second simulation, the inlet stagnation temperatures are 350 K and 300 K for hot and cold passages. The Reynolds number is 168.7 for the upper passage to ensure a Mach number of 0.081 at the upper exit. For the lower passage, the Reynolds number is 170.5 to ensure a Mach number of 0.082 at the lower exit. The exit pressures are imposed to 10^5 Pa for both passages.

Although Miwa et al.[22] present results only for zero thickness solid interface, simulation results are also presented here for a 5 µm solid interface because CHT3D/CFX need a physical solid interface for computations. Here, the solid interface is discretized by 20 nodes in y direction while the nodes spacing in x direction correspond to the passages discretization. The upper passage has a stagnation temperature of 350 K, and the Reynolds number is

1601 to ensure a Mach number of 0.622 at exit. For the lower passage, a stagnation temperature of 300 K is imposed at inlet and the Reynolds number is 196.2 to ensure a Mach number of 0.080 at exit. The thermal conductivity of the plate is 237 W/mK.

Since hot and cold flows are computed separately in ANSYS CFX 12.1, some initial wall boundary conditions have to be imposed to obtain the wall heat fluxes needed by C3D module. The temperature at the solid-hot passage is 320 K, and for the solid-cold passage the temperature is 312 K.

The conjugate heat transfer computation in ANSYS CFX 12.1 assembles computational domains of the hot passage, the cold passage, and the solid. A conservative interface flux is imposed at each solid-fluid interface. The heat flux will go from the boundary side of the fluid to the boundary side of the solid without any loss.
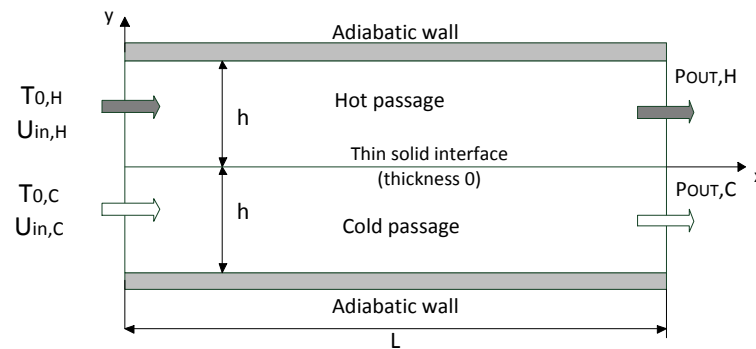
Fig 2   Schematic of parallel-flow.

The second test case proposed from Wright [18] (Fig 3 and Fig 4), is an anti-icing system with three rows of round jets tilted at an angle of -160°. The Wright's experimental data came from the NASA Icing Research Tunnel. Those data are compared with numerical results obtained using an implementation of Goldstein et al. [28] correlation in LEWICE. Experimental data have a jet Reynolds number below the correlation valid range of application. Wright's numerical temperature and heat flux along the leading edge inner wall are computed using LEWICE.

For the internal computational domain used in ANSYS CFX 12.1, jets enter the computational domain from hot air inlet holes of diameter d=1.32 mm and impinge the inner side of the airfoil skin near the leading edge. A uniform velocity, with a Mach number of 0.5, and a uniform temperature of 449.817 K are imposed at inlets. Inlets are located on the inner side of the piccolo tube wall. Thus, the flow follows a small tube, formed by wall thickness, before exiting as a round circular jet with a velocity profile. The piccolo tube has a wall thickness of 1.32 mm and

therefore the ratio of the jet inlet diameter and the tube length is 1. Air exits through channels formed by the inner-liner and the airfoil skin. At the top and the bottom, the channel widths are 0.001 m. The piccolo tube diameter is 0.038 m, and the flow inside the tube is not part of the computational domain. Figure 3 shows the wing and piccolo tube, with a velocity vector swept at an angle of 8° to the z axis. The computational domain used periodic planes, spaced 0.132m apart to reduce computational domain size. A -10 kPa pressure is imposed at channel exits. No-slip boundary conditions are imposed at the piccolo tube wall and at the airfoil skin.

In ANSYS CFX 12.1, the piccolo tube wall is at a constant temperature of 449.817 K, and an adiabatic wall condition is imposed on the inner-liner wall. When calculations are done without coupling with the external flow, a constant temperature of 320 K is imposed on the inner side of the airfoil skin.
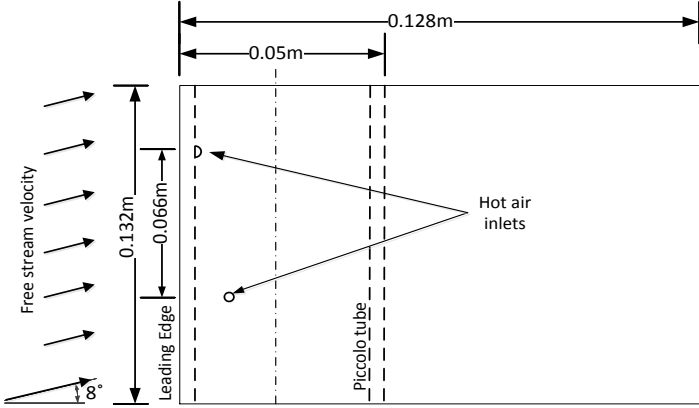
Fig 3   Anti-icing system (top view).
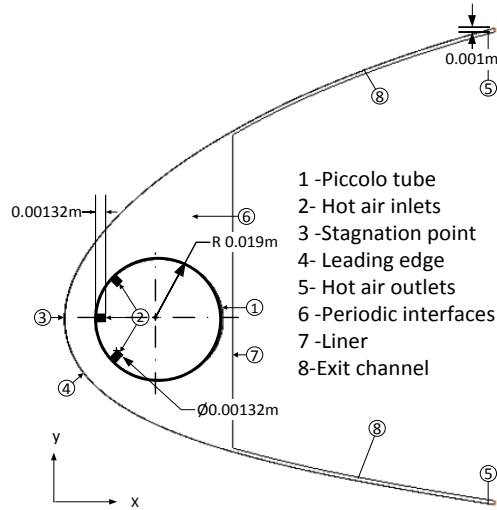
Fig 4   Anti-icing system (side view).

In ANSYS CFX 12.1, the external flow field is representative of a dry airflow cooling an airfoil. Figure 5 illustrates the side and top view of the external flow computational domain. The NACA23014 section is placed at the center of the external domain, and the top view shows the external air velocity sweep angle of 8° to the z axis. A constant low velocity of 59.202 ms^{-1} with a 3° angle of attack is imposed at inlet with a constant inlet temperature of 268.2 K. Periodic boundary conditions are imposed on the two sides of the external domain, thus making it an infinite swept wing. Periodic planes are spaced 0.132 m apart. Opening boundary condition [26] is applied to both top and bottom surface of the external domain.

When calculations are done without coupling with the internal flow, a temperature of 300 K is imposed on the external protected airfoil surface placed in front of the leading edge (4) of Fig 4, and an adiabatic wall condition is imposed everywhere else.

For simplicity reasons, for internal and external flow, a constant turbulence level of 1% and a turbulent viscosity ratio $\mu_t/\mu = 10^{-5}$ are used for calculation of k and ω values at inlet:

$$k_{in} = \frac{3}{2} I^2 U_{in}^2 \tag{21}$$

$$\omega_{in} = \rho \frac{k_{in}}{\mu_t} \tag{22}$$
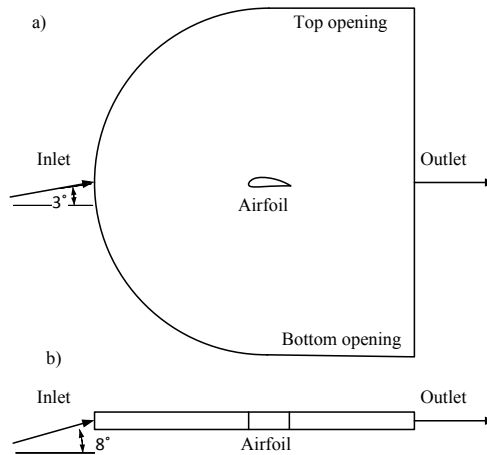
Fig 5   External flow field geometry: a) side view and, b) top view.

IV.   Numerical results

The two-stream parallel flow heat exchanger results are presented first, followed by results for the hot air anti-icing system. Some particular details of the meshes for the internal and external domains are presented. The grid convergence indexes are evaluated for the heat exchanger and the anti-icing system simulations.

For the two-stream parallel flow heat exchanger, for a zero thickness solid interface, numerical bulk temperatures and wall heat fluxes from ANSYS CFX 12.1 are compared to numerical results from Miwa et al.[22]. Numerical results with a finite thickness solid interface are used to compare CHT3D/CFX results to ANSYS CFX 12.1 results.

For the anti-/de-icing system test case, the heat transfer coefficients from ANSYS CFX 12.1 and Wright's numerical results for a dry air case are first compared. Heat transfer coefficients from CHT3D/CFX for a wet air case are compared to conjugate heat transfer results from ANSYS CFX 12.1 and Wright's numerical results for a dry air case. Then, temperature computed with CHT3D/CFX is compared to Wright numerical and experimental results [18].

A. Two-Stream Parallel Flow Heat Exchanger

1)   Case of a zero thickness solid interface

Static temperature contours are plotted in Fig 6 for high velocity in the upper passage combined with low velocity in the lower passage. Arrows show the flow direction. Since the total height (100 µm) is small compared to

the channel length (12 700 μm), only the temperature contours in the zones near the two channel extremities are presented. Clear gray is used for high temperature contours and dark gray is used for low temperature contours. Since the outlet Mach number in hot passage is 0.622, kinetic energy is more important at exit than for cold passage exit, with a Mach number of 0.080. This is why the static temperature is lower in the hot passage than in the cold passage near exit.

The bulk static temperature at a cross section T_b is defined as:

$$T_b = \frac{\int \rho C_p u T dy}{\int \rho C_p u dy} \tag{23}$$
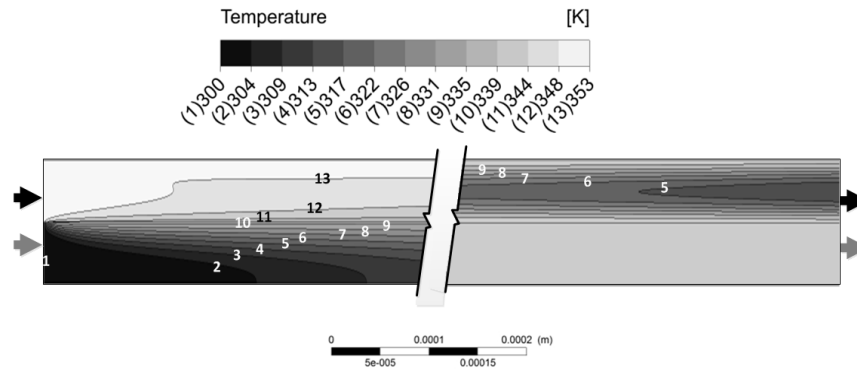
Fig 6   Temperature contours obtained with ANSYS CFX 12.1 for Re_H=1326.4($Ma_{out,H}$=0.622) and Re_C=163.6($Ma_{out,C}$=0.080).

The Fig 7 and Fig 8 compare the bulk temperature evolution against the dimensionless distance x/L for two different Ma and Re numbers in upper passage. ANSYS CFX results for hot and cold passage, named respectively CFX hot and CFX cold, are compared with Miwa et al.[22] results, named respectively ALE hot and ALE cold. The curves intersection at distance x/L=0.35 in Fig 7 is a temperature inversion point. The temperature inversion in both passages is only observed for high velocity flow in hot passage combined with low velocity flow in cold passage.

There is no temperature inversion in the other simulation, as seen in Fig 8 with low velocity flow in hot passage and low velocity flow in cold passage. The temperature evolutions computed with ANSYS CFX 12.1 agree with Miwa et al. [22] results.
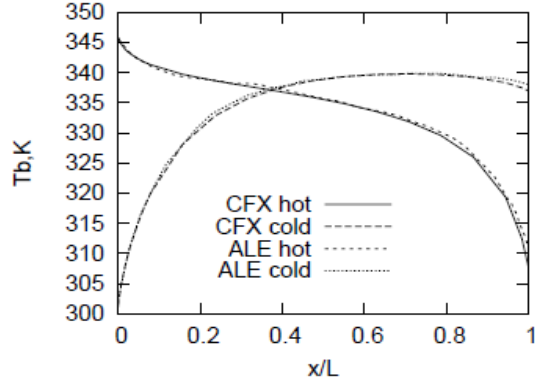
Fig 7 Bulk temperature for Re_H=1326.4 ($Ma_{out,H}$=0.622) and Re_C=163.6 ($Ma_{out,C}$=0.080).
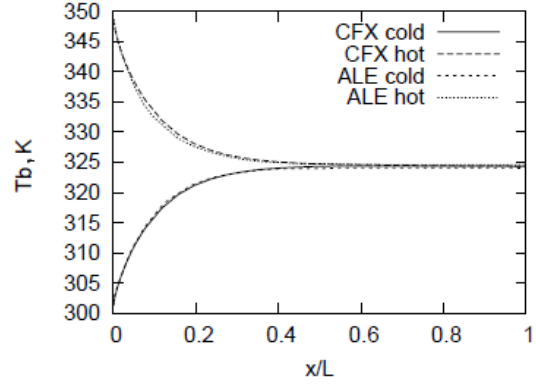
Fig 8 Bulk temperature for Re_H=168.7 ($Ma_{out,H}$=0.081) and Re_C=170.5 ($Ma_{out,C}$=0.082).

A grid refinement study is done following a method suggested by Roache [29] to evaluate the Grid Convergence Index (GCI), representative of the numerical error. The GCI is evaluated using three meshes. The coarser mesh has 400×20 nodes, the same number of nodes used by Miwa et al. [22], the medium mesh has 800×40 nodes and the finer mesh has 1200×60 nodes. Fig 9 shows the wall heat flux at the solid interface plotted against the dimensionless distance x/L. A positive heat flux means that heat enters the cold passage, whereas a negative heat flux means that heat leaves the cold passage. The wall heat flux values obtained with coarse mesh are compared to those obtained with the medium and the fine mesh at the corresponding node. As shown in Fig 9, curves are coincident. The average GCI of the wall heat flux is evaluated to be 0.6373% using the medium mesh.
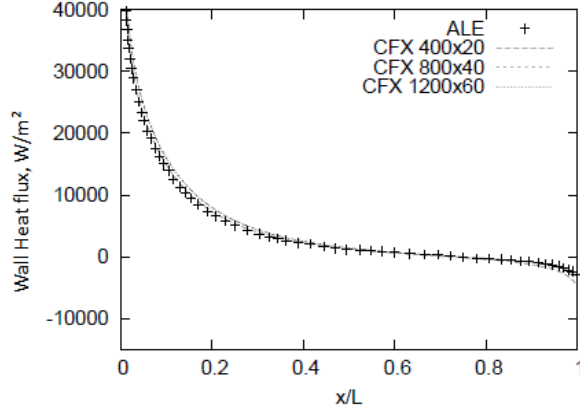
Fig 9 Wall heat flux for 400×20, 800×40 and 1200×60 nodes (without solid)

2) Case of solid interface of finite thickness

Now that ANSYS CFX 12.1 results are validated for a zero thickness solid interface, CHT3D/CFX results are compared with ANSYS CFX 12.1 results for a thick solid interface.

In Fig 10, the wall heat fluxes are plotted against dimensionless distance *x/L*. The wall heat fluxes are plotted for comparison between ANSYS CFX 12.1 (named CFX 12.1) and CHT3D/CFX. The solid-hot passage interface heat flux is designated by $q_{w,H}$ and is plotted in the bottom of the figure. The solid-cold passage interface heat flux is designated by $q_{w,C}$ and is plotted in the top of the Fig 10. For the hot passage, a negative heat flux means that heat leaves the passage. As shown on Fig 10, the results from CHT3D/CFX are in good agreement with the results from ANSYS CFX 12.1.

The relative errors based on the wall heat flux, defined by Eq. **(24)**, are 6.2% and 4.6% for the hot passage interface and for the cold passage. The relative error evolution with x/L is plotted in Fig 11. The error is very small on most of the solid-fluid interfaces. The error seems to be high for the cold passage near the first 10% of the channel, but this is caused by the relative error definition used. The heat fluxes near inlet are high, around 40 000 W/m²K, and are divided by the average heat flux value, an order of magnitude lower.

$$\varepsilon_{realtive}(\%) = \left| \frac{\left(q_{w,CFX} - q_{w,CHT3D/CFX} \right)}{q_{w,CFX}} \right| \times 100 \tag{24}$$

The Fig 12 display the bulk temperature as defined before using Eq. (23). The bulk temperature results are from ANSYS CFX 12.1 and from CHT3D/CFX. This figure is to be compared with Fig 7 results for a zero thickness solid interface. The curve intersection at distance x/L=0.39 is a temperature inversion point. For a zero thickness wall interface, the inversion point was at x/L=0.35. The downstream displacement of the inversion point is resulting from the axial conduction in the solid. For a non zero solid thickness, some of the heat flux coming into the solid from the hot interface does not cross directly to the cold interface but instead it goes in the x direction following temperature gradient inside the solid. Also, this causes a small difference in T_b only for the cold flow near exit. Using Eq. (24) with the bulk temperature from Fig 12 instead of the wall heat flux, the relative error for both hot and cold flow is evaluated to be 0.1%.
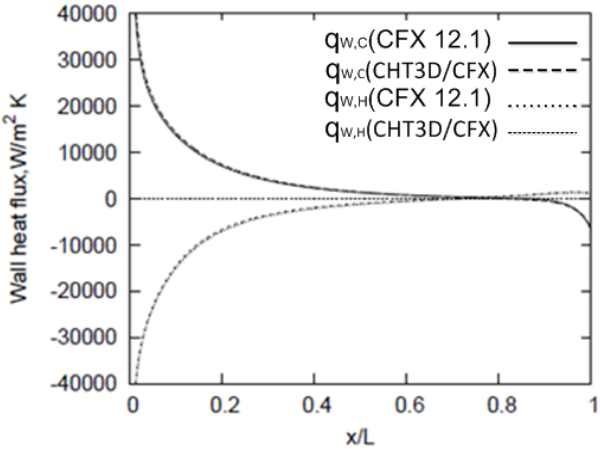
**Fig 10 Wall heat fluxes comparison: CHT3D/CFX and ANSYS CFX 12.1 for 5 μm thick solid interface**
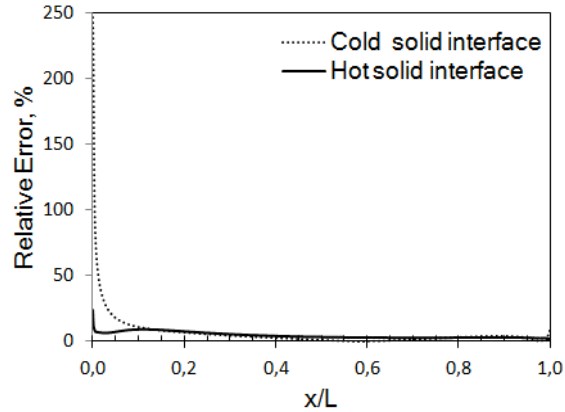
**Fig 11 Relative error on heat fluxes:ANSYS CFX 12.1 vs CHT3D/CFX.**
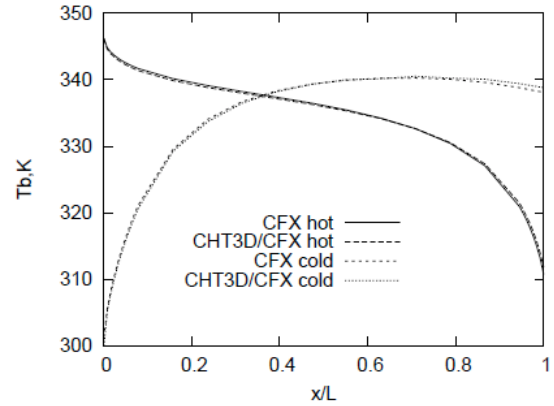
Fig 12 Bulk temperature for Re_H=1601 ($M_{aout,H}$ =0.622) and Re_C=196.2 ($M_{aout,C}$ =0.080) for a 5μm thick solid interface (ANSYS CFX 12.1).

Results from ANSYS CFX 12.1 for a zero thickness solid interface are in good agreement with numerical results from Miwa et al.[22]. Results obtained with the conjugate heat transfer procedure of ANSYS CFX 12.1 using hot high velocity and cold low velocity flows, and solid conduction compared well with CHT3D/CFX for a non-zero solid interface thickness. The CHT3D/CFX procedure will now be used for computation on more complex geometry representative of an anti-icing system where the conjugate heat transfer is performed using internal and external flow and solid conduction in the airfoil skin.

B. Anti-icing system

The selected experimental test case geometry is complex, and some assumptions were needed to achieve the mathematical model. The model uses the ideal gas law assumption for air, the flow is assumed to be steady, and radiations are neglected. The Table 1 lists the test conditions used in IRT experiments [18].

1)   Internal flow

The internal flow geometry is representative of a jet warming an airfoil leading edge. The mesh used is shown on Fig 13. Prismatic element layers are used near all walls, and tetrahedral elements are used elsewhere. To ensure $y^+ \leq 2$, for medium mesh the prism layer thickness is set to 4×10^{-4} m with 20 prismatic layers and a growth ratio of 1.1.

The jet cores are refined from the inlet to the wall in the leading edge area as detailed in Fig 13-*a*. Runback zones in front of the jets and along the airfoil are also refined (Fig 13-*b*).

In Fig 14, two cross-section views are used to plot the streamline velocity contours. The left one contains the jet centerline 1 and the right one contains the jet centerlines 2 and 3. Stagnation, fountain, and reattachment points are also plotted and are represented by ball, octahedron and cube symbols. These points are defined to localize important geometric features used later in heat transfer coefficient figures. Figure 14 shows large vortices aligned with the piccolo tube in upper and lower sides of the jet core.

Table 1 Test conditions

$T_{0.air}$ (K)	268.2
V_{air}(m/s)	59.202
MVD(μm)	29
LWC (g/m^3)	0.87
AOA ($°$)	3
Time (min)	22.5
$\dot{m}_{jet}$ (kg/s)	0.000327394
$T_{0,jet}$(K)	449.817
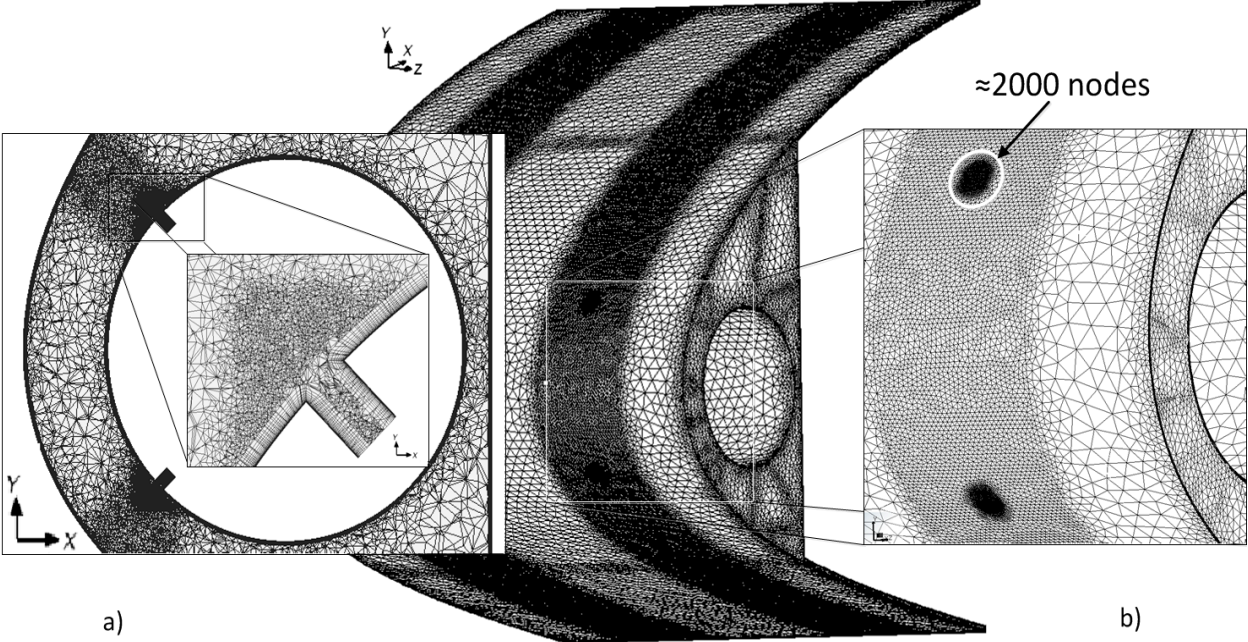
Fig 13 Internal flow domain mesh: a) zoom on jet core refinement region and prism layers; b) front view of the leading edge.

In the same cross-section views, Mach number contours are plotted in Fig 15. Velocity profiles in the three jets prior entering the large computation domain are a results of the non-slip condition imposed in the small cylinders

just after inlets as shown in the zoom of the Fig 15. The flow in the core of the jet is accelerated from $Ma=0.5$ to

0.67 and decelerated to $Ma=0$ at the stagnation points.
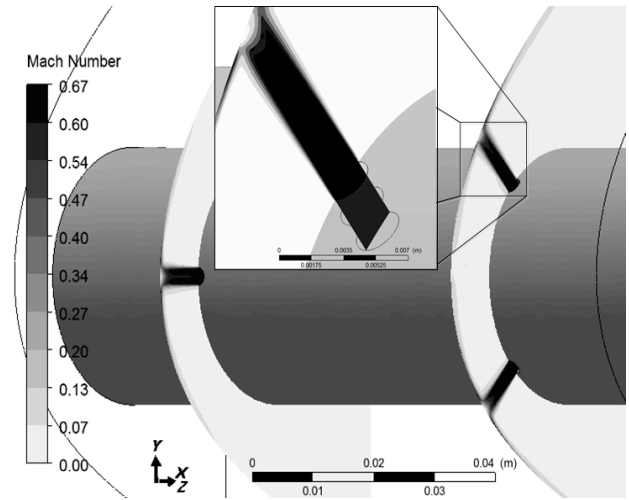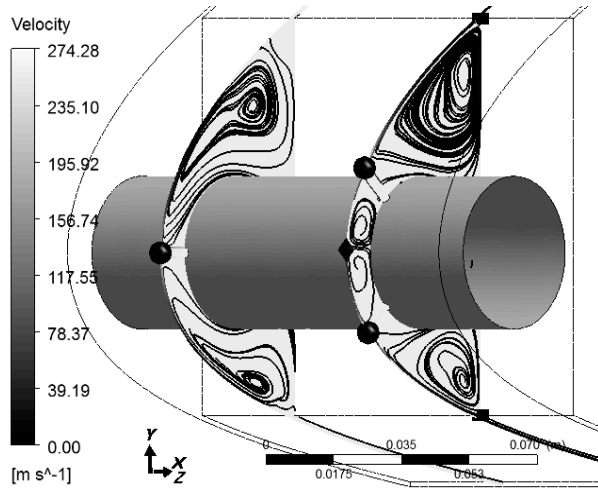
**Fig 14 Velocity streamlines (ANSYS CFX) in two cross-section views.**   **Fig 15 Isocontours of Ma in two cross-section views.**

Regarding the two streams parallel flow heat exchanger of the previous section, a grid refinement study is done

for this case to evaluate the *GCI* for the internal flow. The *GCI* is defined following Roache [29] procedure for

unstructured grid refinement.

$$GCI = \frac{F_s \, |\varepsilon|}{r^p - 1} \tag{25}$$

In the present study, for two grids of spacing h1 and h2, the safety factor $F_s = 3$, the theoretical order of the

method $p = 2$, and the refinement ratio $r = $ h2/h1 $=4$. The relative error ε is defined as

$$\varepsilon = \frac{f_2 - f_1}{f_1} \tag{26}$$

where f is either $\bar{h}(area)$, $\bar{h}(curve)$ or $\bar{h}_{max}(curve)$.

Three meshes are used, keeping the same number of prismatic layers but with a different prism layer thickness. For the finer mesh, the prism layer thickness is 1×10^{-4} m, and for the medium and coarse mesh, it is 4×10^{-4}m, but with 16 prismatic layers for the coarse mesh. The coarser mesh has 3×10^{5} nodes, the medium mesh has 1.5×10^{6} nodes, and the finer mesh has 8×10^{6} nodes.

The *GCI* are evaluated using the area average heat transfer coefficient $\bar{h}(area)$ on the airfoil wall, the curve average, $\bar{h}(curve)$ and the maximal $\bar{h}_{\max}(curve)$ on the curve. The curve is extracted from the airfoil wall intersection with the plan containing the superposed jet centerlines. The local heat transfer coefficient is defined by:

$$h = \frac{q_w}{(T_{wall} - T_{0,jet})} \qquad (27)$$

Table 2 lists different *GCI* values for medium and fine meshes

The curve average *GCI* is evaluated to be 9.24%. The other *GCI* evaluated are shown in Table 2. *GCI* values for different heat transfer coefficient are almost the same and it can be verified that major error occurs in three regions for jet 2 and 3 centerlines results. The first region is at the stagnation regions for $-0.02845 \leq s/c \leq -0.0188$, and $0.1755 \leq s/c \leq 0.0784$-(ball symbol in Fig 14). The *GCI* corresponding for these two stagnation regions are 34% and 14% respectively. The second one is between the two adjacent flows in fountain region (octahedron symbol in Fig 14) at $s/c = 0.0033$. The *GCI* is evaluated to be 16%. The third one occurs at the reattachment points (cube symbol in Fig 14) at $s/c = 0.0784$ and $s/c = -0.0716$ corresponding to the upper and lower inlet channels locations. The corresponding *GCI* for these two points is 15%. The different *GCI* values are quite the same, despite the heat transfer definition used. The *GCI* values are still high for the medium mesh, but given the complexity of the flow, and the other expected numerical errors when coupling with external flow field, the medium mesh will be used to compute the internal flow and the corresponding heat transfer.

The heat transfer coefficients on the internal wall of the airfoil leading edge corresponding to jet 2 and 3 centerline, and jet 1 centerline are plotted in Fig 16 and Fig 17 respectively. The heat transfer coefficients are plotted against the dimensionless distance *s/c*. The zero in Fig 16 corresponds to the fountain point, and it corresponds to the stagnation point in Fig 17. The curves show that the wall heat transfer coefficient reaches maximum values in the

vicinity of the jet stagnation point for -0.035≤ *s/c* ≤ 0.015 and 0.015≤ *s/c* ≤ 0.035 in fig 16 and for -0.015≤ *s/c* ≤ 0.015 in fig 17.

An important observation is made near the stagnation region. A close-up of the stagnation region is shown in the inset in Fig 16 within -0.034 ≤ *s/c* ≤ 0. The grid in this region is refined as shown in Fig 13-b, and the number of nodes in this region are about 2000. The first maximum value occurs a little after the stagnation point for the heat transfer coefficient. A similar phenomenon is also observed in previous jet impingement studies done by Park et al.[30] and Heyerichs. et al.[31]. It occurs when a constant velocity and turbulent profiles are used at jet inlet. The second maximum value is also observed for specific jet entrance to impinging wall spacing. Finally, both heat transfer coefficients from Wright and ANSYS CFX 12.1 increase near channel entrance, around *s/c*=0.075.

ANSYS CFX 12.1 results predict higher heat transfer coefficients than Goldstein correlation. The Goldstein correlation has been derived for a single jet impinging on a straight wall. The correlation parameters are the distance on surface between jet impingement point and local position, jet Reynolds number, and distance between jet entrance and wall. Compressibility effects are not taken into account. Its application to this type of flow where jets interact together has not been validated. However, we will see later that surface temperature predictions are not that much affected by these higher heat transfer coefficients.

Table 2 Different GCI evaluated for two meshes: medium and fine

|	medium	fine	*GCI*
N° nodes	1541505	8×10^6	
$\bar{h}(area)$	2.9268	3.1348	0.0938
$\bar{h}_{max}(curve)$	8.645	9.2122	0.0924
$\bar{h}(curve)$	93.0506	99.0569	0.0910
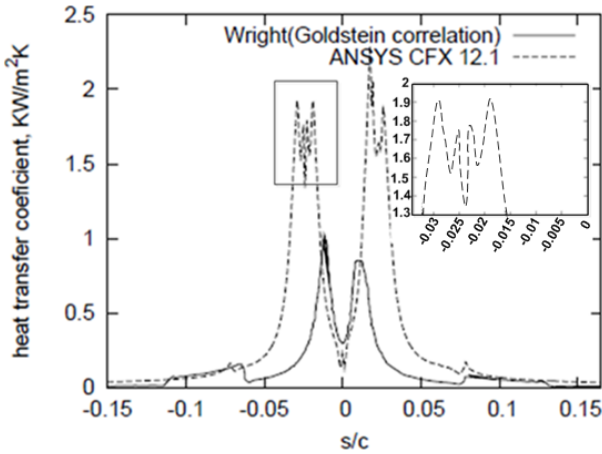
Fig 16 Heat transfer coefficient for internal flow, along a line formed by intersection of inner surface and a plane cutting jet 2 and 3 at centerline.
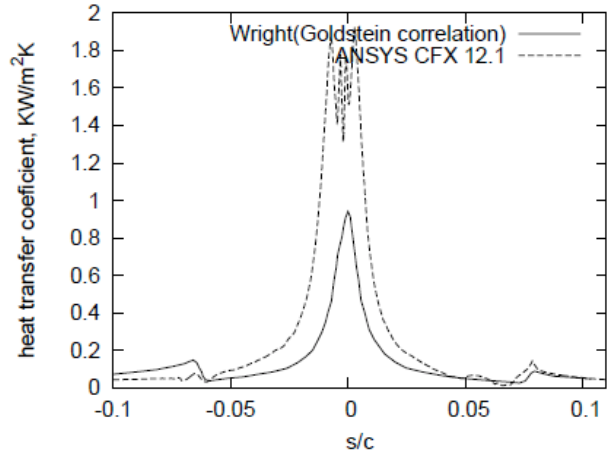
Fig 17 Heat transfer coefficient for internal flow, along a line formed by intersection of inner surface and a plane cutting jet 1 at centerline.

2)   External flow

Figure 18 is a 2D global view of the hexahedral elements used to mesh the external domain with detailed view of the mesh near the airfoil. The external flow is representative of the flow cooling an airfoil at low velocity. The first hexahedral layer near the airfoil wall is located 4×10^{-6} m apart from surface and a growth ratio of 1.1 is applied. The number of nodes in the *x, y, z* direction respectively is $180\times100\times100$. After a solution is obtained, *y+* contours are plotted on the airfoil wall to verify the quality of the near wall mesh (Fig 19). The maximum value, below 1, is located in the leading edge area.

a)

b)

Yplus
Contour 1
0.91
0.83
0.75
0.67
0.59
0.51
0.42
0.34
0.26
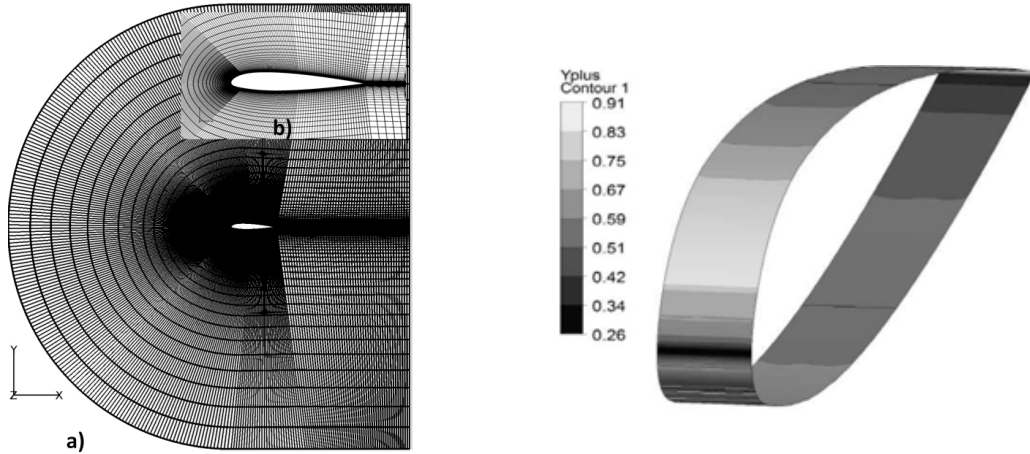
Fig 19 y^+

Fig 18 External mesh with hexahedral elements: a) global view, b) zoom on airfoil.

isocontours (ANSYS CFX 12.1).

Pressure coefficients are plotted in Fig 20 against dimensionless distance x/c, where c is the NACA 23014 airfoil chord. Results are compared to Xfoil [32] results. In Xfoil, the flow is considered viscous with a Reynolds number of 6.9×10^6 and *AOA=3°*. Results from ANSYS CFX 12.1 are in good agreement with data from Xfoil. Except for a small zone on the upper surface around *x/c*=0.1, where discrepancy is apparent. But the swept angle is not taken into account by Xfoil and that may explain the discrepancy.
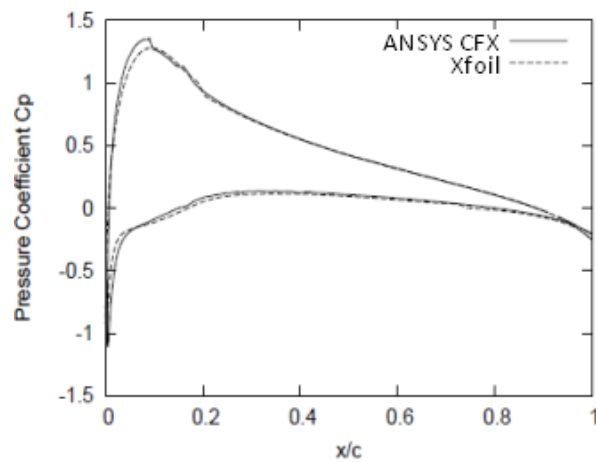

Fig 20 Pressure coefficient *Cp* (ANSYS CFX 12.1 vs Xfoil) *Re*=6.9 × 106, *AOA*=3°.

3) Conjugate heat transfer

In this section, temperature comparisons with experimental data are presented. Thermocouples placed on the inside of the airfoil skin are used to obtain experimental temperatures. Coordinates of the thermocouple locations are listed in Table 3. Temperatures at span wise cross-sections are also compared to experimental and Wright data.

Table 3 Thermocouples locations: cutting plane 1 (left), cutting plane 2 (right)

TC	x(m)	y(m)	z(m)	TC	x(m)	y(m)	z(m)
TL1	0.0483	-0.0390	-0.0058	TL8	0.0467	-0.0385	-0.0038
TL2	0.0272	-0.0316	-0.0287	TL9	0.0259	-0.0311	0.0193
TL3	0.0083	-0.0200	-0.0135	TL10	0.0075	-0.0191	0.0041
TL4	0.0000	0.0008	-0.0211	TL11	0.0000	0.0005	0.0112
TL5	0.0035	0.0175	-0.0211	TL12	0.0033	0.0169	0.0112
TL6	0.0112	0.0330	-0.0135	TL13	0.0105	0.0318	0.0193
TL7	0.0216	0.0467	-0.0287	TL14	0.0204	0.0453	0.0041
				TL14	0.0321	0.0576	0.0269

Heat transfer coefficients obtained for curvilinear axis aligned with the center jet span wise location are presented in figure 23 and 24. According to the test conditions from Table 1, the heat transfer coefficients computed with CHT3D/CFX are compared to the ones from Wright [18] and conjugate heat transfer numerical results from ANSYS CFX 12.1. The ANSYS CFX 12.1 conjugate heat transfer is computed without droplet impingement and ice accretion. The span wise heat transfer coefficient values are plotted against the dimensionless distance s/c. The zoom in Fig 23 shows the heat transfer coefficient at stagnation point along a line formed by intersection of inner surface and a plane cutting jet 2 and 3 at centerline.

The flow is quite complex, with large recirculation areas, as shown earlier in Fig 14. They cause an increase in heat transfer in the stagnation areas, because of the fluid acceleration. CHT3D/CFX predicts higher heat transfer than Wright in the impingement areas. The jet stagnation point from CHT3D/CFX seems to be slightly shifted from Wright's jet stagnation points, but it is hard to tell because of the higher heat transfer values. The stagnation area seems also larger in the s/c direction. CHT3D/CFX predicts the same heat transfer coefficients than Wright in the areas from $-0.151 \leq s/c \leq -0.0716$ and $0.0784 \leq s/c \leq -0.163$ for the jet 2 and 3 centerline span wise location. The same comment can be said for the jet 1 centerline span wise location.

An example of the numerical temperature isocontour map obtained with CHT3D/CFX at a cross section (z=-0.33m) of jet 2 and 3 centerline is presented in Fig 21. Temperature contour map on the airfoil leading edge obtained with CHT3D/CFX in isometric view is shown in Fig 22. Figure 21 shows the static temperature contours with the

external, internal, and solid domains computed by CHT3D/CFX. Each contour domain has his own colormap gray scale. The zoom view in Fig 21 focuses on both solid-fluid interfaces during the conjugate heat transfer using CHT3D/CFX. The maximum temperature reached at the internal skin of the airfoil is 333 K and 268 K at the external skin. Maximum temperature occurs at the jet stagnation area on the airfoil wall. The isocontours are perpendicular to the airfoil walls not close to the jet stagnation area, indicating that energy is removed from the stagnation areas by conduction inside the airfoil skin.

Those figures show the capability of the new module CHT3D/CFX to evaluate the conjugate heat transfer. The heat transfer coefficients are calculated over all the 3D airfoil skin during the conjugate heat transfer computation instead of using imposed values from correlation on the internal side.

The ANSYS CFX 12.1 and the CHT3D/CFX results are in good agreement. The CHT3D/CFX procedure computes the internal wall heat flux from ANSYS CFX 12.1 but considers the interaction with ICE3D runback water film calculation. The heat transfer from ANSYS CFX 12.1 is computed in dry mode, without runback water film. ANSYS CFX 12.1 predicts higher heat transfer coefficients than CHT3D/CFX but that does not mean that heat fluxes are higher. The heat transfer coefficient definition divides heat flux by the difference between locally inner wall temperature and jet temperature. Although not shown here, the wall temperatures are colder when water runback is present.
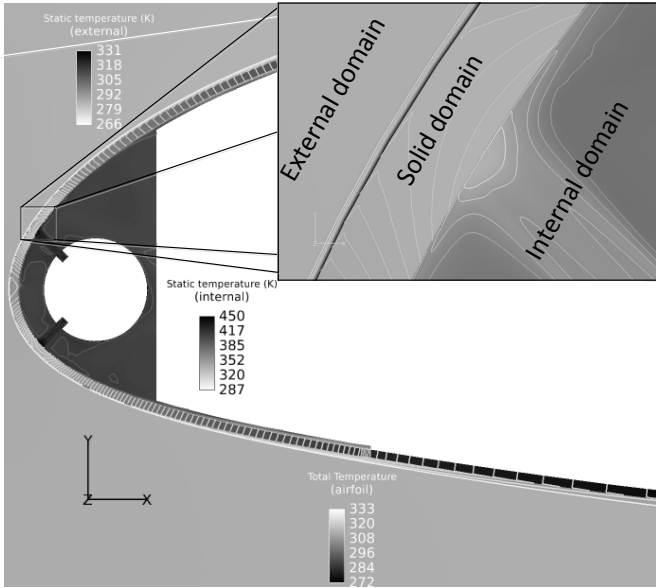
Fig 21 Numerical isocontour map of the static temperature at a cross-section cutting jet 2 and 3 at centerline.
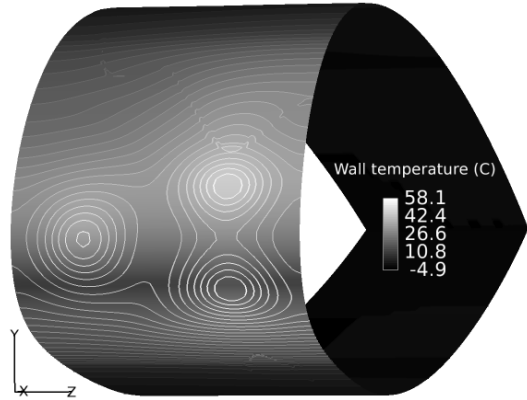
**Fig 22 Numerical isocontour map of the wall temperature (C).**
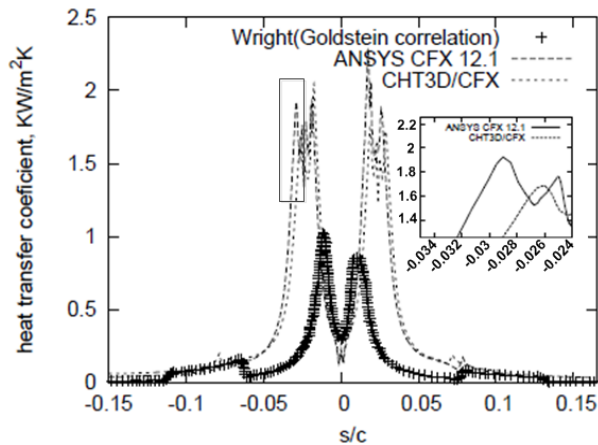
Fig 23 Heat transfer coefficient along a line form by intersection of inner surface and a plane cutting jet 2 and 3 at centerline (CHT3D/CFX, CFX 12.1 and Wright).
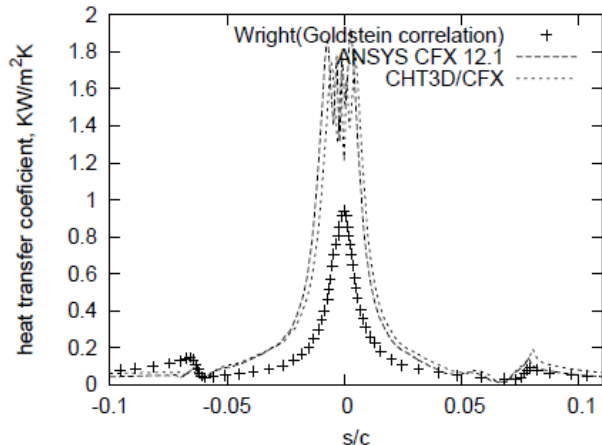
Fig 24 Heat transfer coefficient along a line form by intersection of inner surface and a plane cutting jet 1 at centerline(CHT3D/CFX, CFX 12.1 and Wright).

Figures 25 and 26 compare temperature extracted from the internal wall at the airfoil leading edge at two experimental span cross-sections according to Table 3. The temperature distribution from CHT3D/CFX is compared to that from Wright numerical results and experimental data [18]. The lines in these figures represent interpolated value between the measure points. At the same span cross-sections according to Table 3, figures 27 and 28 compare

wall heat flux and heat transfer coefficient from CHT3D/CFX and Wright numerical results. Because of the numerical and experimental errors, temperature profiles on the span cross-section locations are not exactly matched. The temperature profiles at span cross-section 1 and at span cross-section 2 are similar, and are between 295 K and 325 K. CHT3D/CFX temperatures at span cross-section 1 are higher than experimental values. CHT3D/CFX temperatures at span cross-section 2 are in good agreement with experimental and Wright numerical data. Because the CHT3D/CFX predicted internal heat transfer coefficients are higher than the ones used by Wright as shown in Fig. 27 and 28, the predicted wall temperatures are lower. The Fig. 27 and 28 also present the wall heat fluxes on the right axis. The left and right axis scales are selected such that, for CHT3D/CFX, the heat transfer coefficients and the wall heat flux curves are juxtaposed. Surface temperature variations are small compared to heat transfer coefficient denominator, $T_{wall} - T_{0,jet}$. The runback water film and the external flow heat transfer coefficients may be more critical for surface temperature prediction, but further investigations with other turbulent models such as LES are needed.
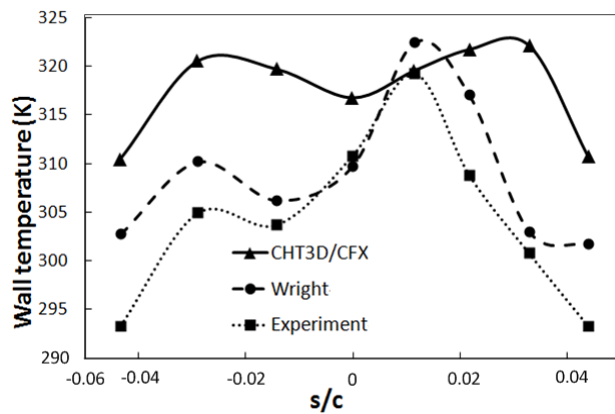

**Fig 25 Temperature comparison: CHT3D/CFX vs LEWICE and Experimental-at span cross-section 1 location.**
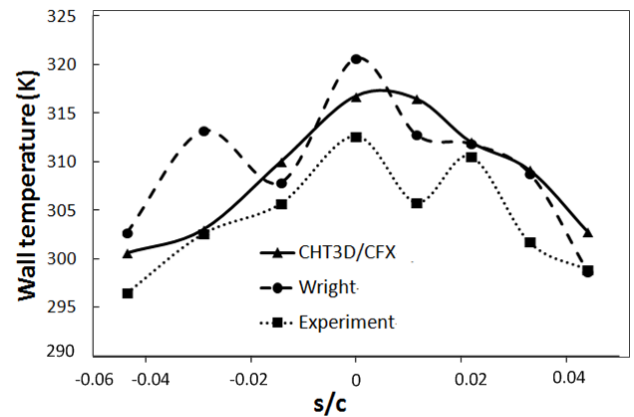
Fig 26 Temperature comparison: CHT3D/CFX vs LEWICE and Experimental-at span cross-section 2 location.
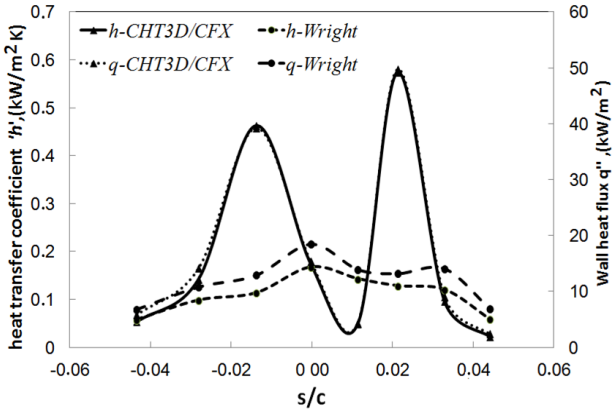
Fig 27 Wall heat flux and heat transfer coefficient comparison: CHT3D/CFX vs LEWICE at span cross-section 1 location.
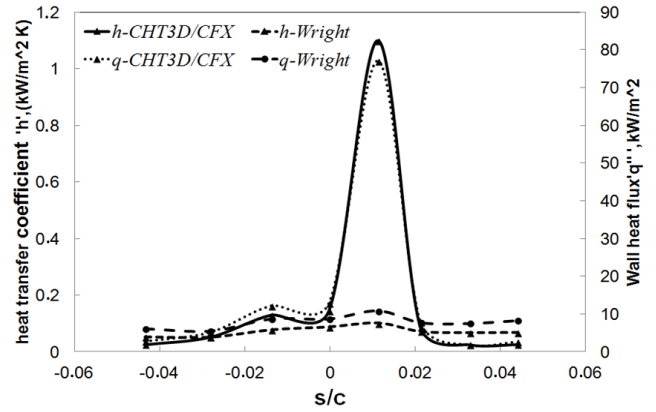
Fig 28 Wall heat flux and heat transfer coefficient comparison: CHT3D/CFX vs LEWICE at span cross-section 2 location

V.   Conclusion

Using commercial CFD codes, FENSAP-ICE and ANSYS CFX 12.1, and a new procedure CHT3D/CFX, the heat transfer coefficients and the temperatures are calculated using conjugate heat transfer methodologies. The results are compared with literature data to validate the new CHT3D/CFX procedure.   For parallel flow heat exchanger, conjugate heat transfer results compare well with numerical results from literature. For a piccolo tube anti-icing system and a particular airfoil shape exposed to wet airflow, conjugate heat transfer results are presented. Although the flow is complex, numerical results agree with literature. For wet air case, numerical temperatures are compared to experimental results at corresponding locations. They are also compared to other numerical results. CHT3D/CFX temperatures are close to the experimental temperature, even if the computed internal coefficients of heat transfer are higher than the ones predicted by a correlation used in literature.

Acknowledgments

References

[1]   Papadakis, M. and Wong, S.-H. J., "Parametric investigation of a bleed air ice protection system", *44th AIAA Aerospace Sciences Meeting*, Reno, NV, 2006, pp. 12167-12194.
         doi: 10.2514/6.2006-1013

[2]   Bourgault, Y., Habashi, W. G., Dompierre, J. and Baruzzi, G. S. "A finite element method study of Eulerian droplets impingement models". *International Journal for Numerical Methods in Fluids,* Vol. 29, No. 4, 1999, pp. 429, 449.
         doi: 10.1002/(SICI)1097-0363(19990228)29:4<429::AID-FLD795>3.0.CO;2-F

[3]   Bourgault, Y., Beaugendre, H. and Habashi, W. G. "Development of a shallow-water icing model in FENSAP-ICE". *Journal of Aircraft,* Vol. 37, No. 4, 2000, pp. 640, 646.
   doi: 10.2514/2.2646

[4]   Beaugendre, H., Morency, F., Habashi, W. G. and Benquet, P. "Roughness implementation in FENSAP-ICE: Model calibration and influence on ice shapes". *Journal of Aircraft,* Vol. 40, No. 6, 2003, pp. 1212, 1215.
   doi: 10.2514/2.7214

[5]   Habashi , W. G., Martin , A., Guido , B., François , M., Pascal , T. and Narramore , J. C., "FENSAP-ICE: a Fully-3D in-Flight Icing Simulation System for Aircraft, Rotorcraft and UAVS", *24th International Congress of The Aeronautical Sciences* 2004.
   doi:

[6]   Honsek, R., Habashi, W. G. and Aube, M. S. "Eulerian modeling of in-flight icing due to supercooled large droplets". *Journal of Aircraft,* Vol. 45, No. 4, 2008, pp. 1290, 1296.
   doi: 10.2514/1.34541

[7]   Remaki, L., Beaugendre, H. and Habashi, W. G. "ISOD – an anisotropic isovalue-oriented diffusion artificial viscosity for the Euler and Navier–Stokes equations". *Journal of Computational Physics,* Vol. 186, No. 1, 2003, pp. 279, 294.
   doi: 10.1016/S0021-9991(03)00066-4

[8]   Zuckerman, N. and Lior, N. "Jet Impingement Heat Transfer: Physics, Correlations, and Numerical Modeling". *Advances in Heat Transfer,* Vol. 39,2006, pp. 565, 631.
   doi: 10.1016/S0065-2717(06)39006-5

[9]   Hannat, R., "Etude numerique des effets de la compressibilite sur le transfert de chaleur dans un systeme antigivre a air chaud," MR52791 M.Ing., Ecole de Technologie Superieure (Canada), Montreal, 2009.

[10]   Brown, J. M., Raghunathan, S., Watterson, J. K., Linton, A. J. and Riordon, D. "Heat transfer correlation for anti-icing systems". *Journal of Aircraft,* Vol. 39, No. 1, 2002, pp. 65-70.
   doi: 10.2514/2.2896

[11]   Croce, G. F., Habashi, W. G., Guevremont, G. and Tezok, F., "3D thermal analysis of an anti-icing device using FENSAP-ICE", *36th AIAA Aerospace Sciences Meeting and Exhibit*, Reno, NV, 1998.
   doi: 10.2514/6.1998-193

[12]   Fregeau, M., Gabr, M., Paraschivoiu, I. and Saeed, F. "Simulation of heat transfer from hot-air jets impinging a three-dimensional concave surface". *Journal of Aircraft,* Vol. 46, No. 2, 2009, pp. 721, 725.
   doi: 10.2514/1.39846

[13]   Saeed, F. "Numerical simulation of surface heat transfer from an array of hot-air jets". *Journal of Aircraft,* Vol. 45, No. 2, 2008, pp. 700, 714.
   doi: 10.2514/1.33489

[14]   Morency, F. and Hannat, R., "Numerical Prediction of Heat Transfer in the Case of a Heated Leading Edge", *AIAA Atmospheric and Space Environments*, Toronto, Aug 2010.
   doi: 10.2514/6.2010-7836

[15]   Papadakis, M., Wong, S. H., Yeong, H. W., Wong, S. C. and Vu, G. T., "Icing Tests of a Wing Model with a Hot-Air Ice Protection System", *AIAA Guidance, Navigation, and Control Conference*, Toronto, Aug 2010.
   doi: 10.2514/6.2010-7833

[16]   Domingos, R. H., Papadakis, M. and Zamora, A. O., "Computational Methodology for Bleed Air Ice Protection System Parametric Analysis", *AIAA Guidance, Navigation, and Control Conference*, Toronto, Aug 2010.
   doi: 10.2514/6.2010-7834

[17]   Ghenai, C. and Lin, C. X. "Verification and validation of NASA LEWICE 2.2 icing software code". *Journal of Aircraft,* Vol. 43, No. 5, 2006, pp. 1253, 1258.
   doi: 10.2514/1.18977

[18]   Wright, W. B., "An evaluation of jet impingement heat transfer correlations for piccolo tube application", *42nd AIAA Aerospace Sciences Meeting and Exhibit*, Reno, Nevada, Jan 2004, pp. 4153- 4162.
   doi: 10.2514/6.2004-62

[19]   Carlos N. Donatti, Rafael A. Silveira, Gerson Bridi, Clovis R. Maliska and António F. C. da Silva, "Ice Accretion Simulation in Presence of a Hot Air Anti-Icing System", *19th International Congress of Mechanical Engineering*, Brasília, Nov 2007.
   doi:

[20]   Dong , W., Zhu , J., Zhou , Z. and Chi , X., "Heat Transfer and Temperature Analysis of an Anti-icing System for an Aero-engine Strut under Icing Condition", *43rd AIAA Thermophysics Conference*, New Orleans, Louisiana, Jun 2012.
   doi: 10.2514/6.2012-2753

[21]   Pourbagian , M. and Habashi , G. W., "Parametric Analysis of Energy Requirements of In-Flight Ice Protection Systems", *The 20th Annual Conference of the CFD Society of Canada (CFD2012)*, Canmore, AB, May 2012.
   doi:

[22]   Miwa, J., Asako, Y., Hong, C. and Faghri, M. "Performance of Gas-to-Gas Micro-Heat Exchangers". *Journal of Heat Transfer,* Vol. 131, No. 5, 2009, pp. 1, 9.
   doi: 10.1115/1.3013828

[23]   Reid, T., Baruzzi, G. S., Aliaga, C., Aubé, M. S. and Habashi, W. G., "FENSAP-ICE: Application of Unsteady CHT to De-icing Simulations on a Wing with Inter-cycle Ice Formation", *AIAA Guidance, Navigation, and Control Conference*, Toronto, Aug 2010.
          doi: 10.2514/6.2010-7835

[24]   Messinger, B. L. "Equilibrum Temperature of an Unheated Icing Surface as a Function of Airspeed". *Journal of Aeronautical Sciences,* Vol. 20, No. 1, 1953, pp. 29-42.

[25]   Beaugendre, H., Morency, F. and Habashi, W. G. "Development of a second generation in-flight icing simulation code". *Journal of Fluids Engineering, Transactions of the ASME,* Vol. 128, No. 2, 2006, pp. 378, 387.
          doi: 10.1115/1.2169807

[26]   ANSYS®, ANSYS CFX Release Notes, 12.1 ANSYS, Inc, Canonsburg 2009.

[27]   Menter, F. R. "Two-equation eddy-viscosity turbulence models for engineering applications". *AIAA Journal,* Vol. 32, No. 8, 1994, pp. 1598, 605.
          doi: 10.2514/3.12149

[28]   Goldstein, R. J., Behbahani, A. I. and Heppelmann, K. K. "Streamwise distribution of the recovery factor and the local heat transfer coefficient to an impinging circular air jet". *International Journal of Heat and Mass Transfer,* Vol. 29, No. 8, 1986, pp. 1227, 1235.
          doi: 10.1016/0017-9310(86)90155-9

[29]   Roache, P. J. "Perspective: a method for uniform reporting of grid refinement studies". *Journal of Fluids Engineering, Transactions of the ASME,* Vol. 116, No. 3, 1994, pp. 405-413.
          doi: 10.1115/1.2910291

[30]   Park, T. H., Choi, H. G., Yoo, J. Y. and Kim, S. J. "Streamline upwind numerical simulation of two-dimensional confined impinging slot jets". *International Journal of Heat and Mass Transfer,* Vol. 46, No. 2, 2003, pp. 251, 262.
          doi: 10.1016/S0017-9310(02)00270-3

[31]   Heyerichs, K. and Pollard, A. "Heat transfer in separated and impinging turbulent flows". *International Journal of Heat and Mass Transfer,* Vol. 39, No. 12, 1996, pp. 2385, 2400.
          doi: 10.1016/0017-9310(95)00347-9

[32]   XFOIL, Drela , M. Youngren , H. , 6.9 MIT, 2001.